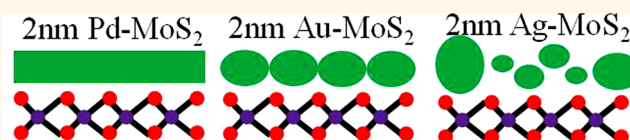


# Metal Contacts on Physical Vapor Deposited Monolayer MoS<sub>2</sub>

Cheng Gong,<sup>†</sup> Chunming Huang,<sup>‡</sup> Justin Miller,<sup>†</sup> Lanxia Cheng,<sup>†</sup> Yufeng Hao,<sup>§</sup> David Cobden,<sup>‡</sup> Jiyoung Kim,<sup>†</sup> Rodney S. Ruoff,<sup>§</sup> Robert M. Wallace,<sup>†</sup> Kyeongjae Cho,<sup>†</sup> Xiaodong Xu,<sup>‡</sup> and Yves J. Chabal<sup>†,\*</sup>

<sup>†</sup>Department of Materials Science and Engineering, The University of Texas at Dallas, Richardson, Texas 75080, United States, <sup>‡</sup>Department of Physics, University of Washington, Seattle, Washington 98195, United States, and <sup>§</sup>Department of Mechanical Engineering and the Materials Science and Engineering Program, The University of Texas at Austin, Austin, Texas 78712, United States

**ABSTRACT** The understanding of the metal and transition metal dichalcogenide (TMD) interface is critical for future electronic device technologies based on this new class of two-dimensional semiconductors. Here, we investigate the initial growth of nanometer-thick Pd, Au, and Ag films on monolayer MoS<sub>2</sub>. Distinct growth morphologies are identified by atomic force microscopy: Pd forms a uniform contact, Au clusters into nanostructures, and Ag forms randomly distributed islands on MoS<sub>2</sub>. The formation of these different interfaces is elucidated by large-scale spin-polarized density functional theory calculations. Using Raman spectroscopy, we find that the interface homogeneity shows characteristic Raman shifts in E<sub>2g</sub><sup>1</sup> and A<sub>1g</sub> modes. Interestingly, we show that insertion of graphene between metal and MoS<sub>2</sub> can effectively decouple MoS<sub>2</sub> from the perturbations imparted by metal contacts (*e.g.*, strain), while maintaining an effective electronic coupling between metal contact and MoS<sub>2</sub>, suggesting that graphene can act as a conductive buffer layer in TMD electronics.



**KEYWORDS:** molybdenum disulfide · metal contact · homogeneity · atomic force microscopy · Raman spectroscopy · graphene · buffer layer

Molybdenum disulfide (MoS<sub>2</sub>) is a transition metal dichalcogenide (TMD) that consists of covalently bonded S–Mo–S sandwiched layers, held together through interlayer van der Waals (vdW) interactions. Increased interest in MoS<sub>2</sub> for electronics has arisen since the experimental demonstration of single-layer MoS<sub>2</sub> transistors with excellent electrical performance,<sup>1–4</sup> namely,  $\sim 10^8$  on/off current ratio and the suggested high carrier mobility.

An outstanding challenge for realizing the application potential of MoS<sub>2</sub> is to engineer Ohmic contact.<sup>2,5,6</sup> Intimate contact between metal and MoS<sub>2</sub> is essential for achieving a high-quality electrical contact to maximize electronic injection, enhance heat dissipation, and improve mechanical properties of devices.<sup>7,8</sup> However, metal deposition on single-layer planar surfaces such as graphene or TMDs may exhibit different degrees of clustering,<sup>7</sup> depending on the relative strengths between adsorbate–substrate and adsorbate–adsorbate interactions. For example, transition metals deposited on graphene tend to cluster.<sup>9–11</sup> Therefore, it is reasonable to expect that clustering may occur as well on MoS<sub>2</sub>

depending on the metal. For instance, Pd as a d-electron metal and Au and Ag as s-electron metals are expected to interact differently with MoS<sub>2</sub>.<sup>12–14</sup>

The deposition of metal contacts may also affect the structure and electronic properties of MoS<sub>2</sub> substantially.<sup>15,16</sup> The high reactivity of metal atoms involved in the deposition process can strongly perturb the phonons and electrons in a monolayer MoS<sub>2</sub> film. It is therefore important to investigate the initial growth of metal deposition to better understand and control the electronic transport and heat dissipation in the nanoscale MoS<sub>2</sub> devices. It is essential to achieve uniform wetting of MoS<sub>2</sub> surface by metal electrodes without modification of the MoS<sub>2</sub> performance for the efficient transport of electrons and phonons within the devices. In this work, we aim to investigate the starting growth modes of different metals on MoS<sub>2</sub>, study the impacts of deposited metal morphologies on the structural and electronic properties of MoS<sub>2</sub>, and suggest practical ways to optimize the metal–MoS<sub>2</sub> contacts, such as by insertion of a graphene layer between metal and MoS<sub>2</sub>.

\* Address correspondence to chabal@utdallas.edu.

Received for review October 7, 2013 and accepted November 12, 2013.

Published online November 12, 2013  
10.1021/nn4052138

© 2013 American Chemical Society

## RESULTS AND DISCUSSION

Single-layer MoS<sub>2</sub> samples are obtained by evaporating MoS<sub>2</sub> powders on 285 nm thick SiO<sub>2</sub> substrate through vapor–solid growth as detailed in the Experimental and Theoretical Methods section. This method provides high-quality single-layer MoS<sub>2</sub> film with near-unity valley polarization.<sup>17</sup> Three different metals (Pd, Au, and Ag) are then deposited using a standard clean-room Temescal evaporator with 10<sup>−6</sup> Torr base pressure. The growth morphologies of each metal are examined by atomic force microscopy (AFM) after deposition of 2 nm average thickness, estimated by a quartz crystal monitor, and the spectral modification of the MoS<sub>2</sub> phonons are examined by Raman spectroscopy.

Figure 1a shows the optical image of the single-layer MoS<sub>2</sub> flakes with triangular shape. The crystal size ranges from several micrometers to tens of micrometers, which is much larger than the laser spot size of 0.6 μm and allows for spatially statistical Raman study. Figure 1b shows a representative Raman spectrum. The measured 18.15 cm<sup>−1</sup> separation between E<sub>2g</sub><sup>1</sup> and A<sub>1g</sub> Raman peaks<sup>17</sup> provides direct evidence for monolayer flakes.<sup>18,19</sup> While the overall behavior of the phonon modes in MoS<sub>2</sub> is well-described in the

community, the effect of metallic films (and also gate dielectrics, and even other dissimilar two-dimensional materials<sup>20</sup>) on phonons has not been studied, despite its direct relevance to realistic electronic devices.

We first use AFM to image the surface morphology of metal deposited on single-layer MoS<sub>2</sub>. The three types of e-beam-evaporated metals (Pd, Au, and Ag) with an average thickness of 2 nm (Figure 2a–c) are studied. We find that Pd wets MoS<sub>2</sub> with rms roughness of ~0.18 nm, while Au assembles in ordered clusters with rms roughness of ~0.36 nm and Ag produces the roughest morphology with a random distribution of islands/clusters of varying sizes with rms roughness of ~0.78 nm. The line profiles for Figure 2a–c suggest that Pd follows a Frank–van der Merwe (FM: layer by layer) growth (*i.e.*, uniform), whereas Au and Ag obey a Volmer–Weber (VW: island formation) instead of a Stranski–Krastanov (SK: layer-plus-island/cluster) growth. While a VW growth is clear for Ag, it is difficult to rule out that clustering is not occurring on top of a thin uniform wetting layer (SK) for Au solely on the basis of AFM images.

The AFM image in Figure 2b shows the presence of holes among dense Au clusters, and the line profile

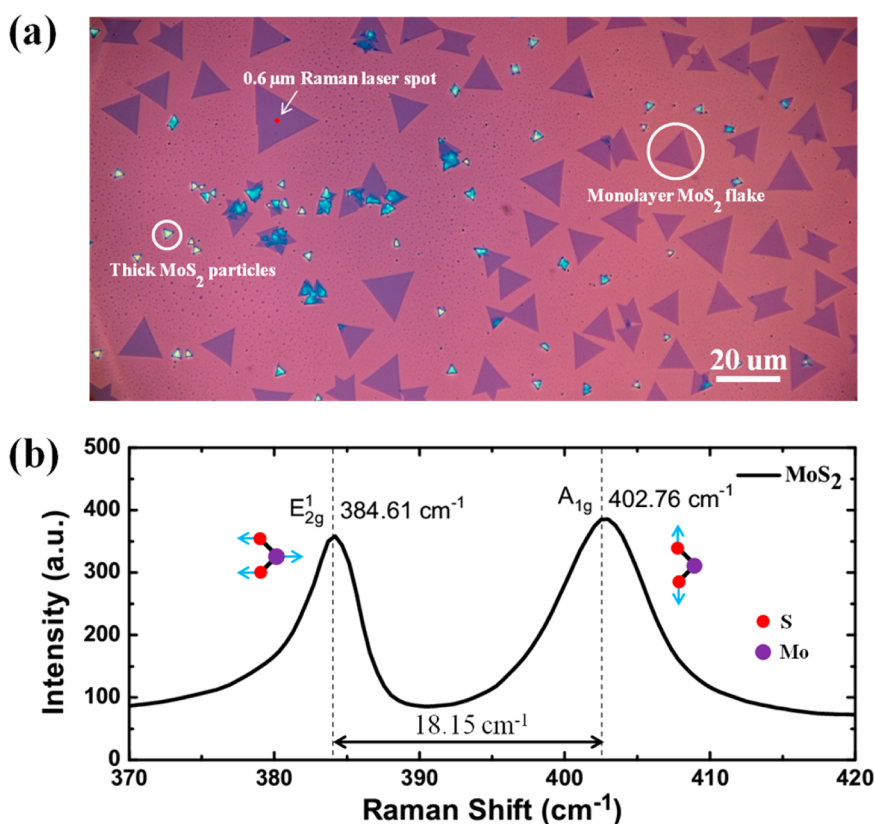


Figure 1. (a) Optical image of single-layer MoS<sub>2</sub> flakes evaporated on 285 nm SiO<sub>2</sub>, and (b) representative Raman spectrum acquired in single-layer MoS<sub>2</sub> flake. The triangular shapes with deep contrast in (a) are monolayer MoS<sub>2</sub> flakes. Raman laser spot is of 0.6 μm diameter, as depicted by the red dot within a MoS<sub>2</sub> flake in (a). Some small size thick MoS<sub>2</sub> particles are also found. The peak positions of the E<sub>2g</sub><sup>1</sup> and A<sub>1g</sub> modes of the bare monolayer MoS<sub>2</sub> flakes are 384.61 cm<sup>−1</sup> (with a standard deviation 0.26 cm<sup>−1</sup>) and 402.76 cm<sup>−1</sup> (with a standard deviation 0.24 cm<sup>−1</sup>), respectively. An averaged 18.15 cm<sup>−1</sup> separation (with a standard deviation 0.34 cm<sup>−1</sup>) between E<sub>2g</sub><sup>1</sup> and A<sub>1g</sub> modes verifies that the MoS<sub>2</sub> flakes are monolayer. The vibration modes of E<sub>2g</sub><sup>1</sup> and A<sub>1g</sub> are illustrated in the insets of (b).

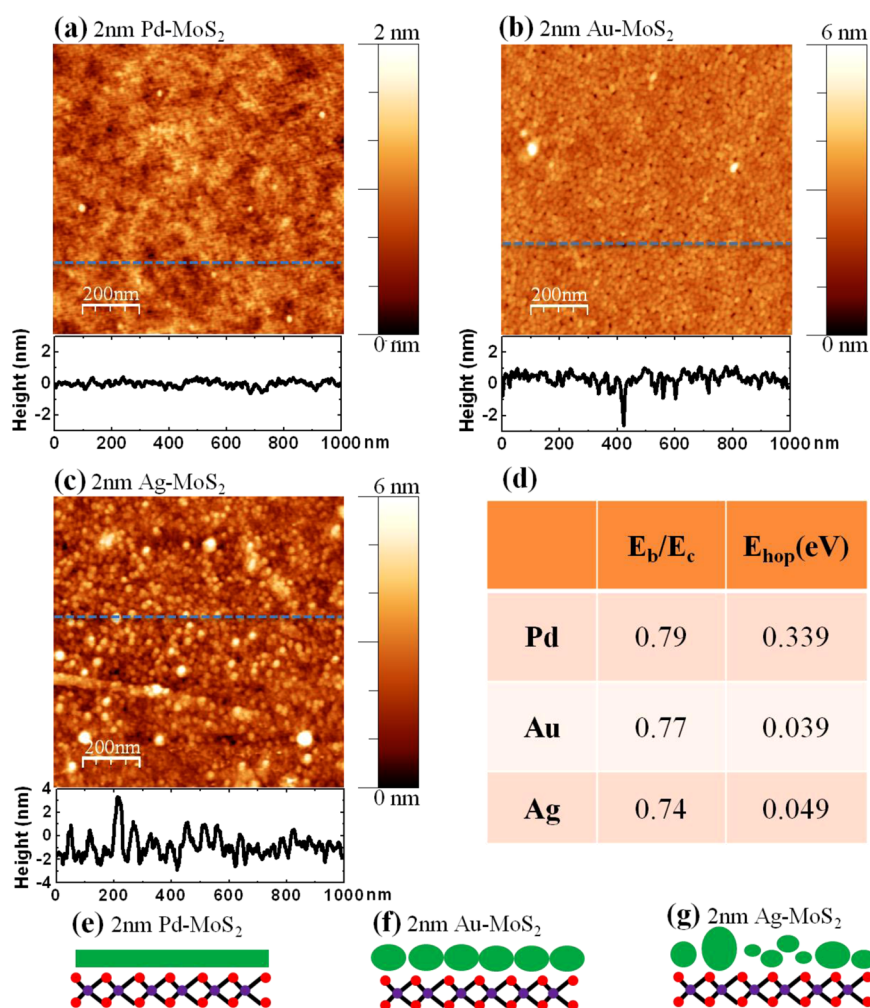


Figure 2. AFM images of 2 nm (a) Pd, (b) Au, and (c) Ag on monolayer MoS<sub>2</sub>. The rms values of roughness are (a) 0.18 nm, (b) 0.36 nm, and (c) 0.78 nm. (d) Calculated binding energy ( $E_b$ ) and cohesive energy ( $E_c$ ) ratio for three different metals on MoS<sub>2</sub>, and the hopping barriers ( $E_{hop}$ ) of metal adatoms on MoS<sub>2</sub>. (e–g) Illustrations of the interfaces of (a–c). The illustrations in (e–g) are not to scale.

shows that the depth of the holes is more than the 2 nm thickness average of the layer, suggesting the absence of uniform wetting layers between the Au clusters and MoS<sub>2</sub>. Moreover, lots of such pinholes can be seen in the magnified AFM image of the Au-MoS<sub>2</sub> sample in Figure S1 (Supporting Information), supporting a VW growth mode. However, these observations are not fully conclusive. The conclusion that Au follows a VW growth mode will be precisely established by the Raman spectra shown below. In summary, while Pd forms a uniform intimate contact with MoS<sub>2</sub>, as illustrated in Figure 2e, Au and Ag tend to cluster on MoS<sub>2</sub>, as illustrated in Figure 2f,g. For a VW growth, such inhomogeneity will lead to regions of intimate contact (between clusters and the MoS<sub>2</sub> substrate) and regions with a notable separation at the edges of clusters (even when neighboring clusters are touching mutually).

Large-scale spin-polarized density functional theory (DFT) calculations are carried out to understand the origin of different metal growth modes on monolayer MoS<sub>2</sub>. Clustering of adsorbates on surfaces is known to

depend on the relative magnitudes of inter-adsorbate and adsorbate–substrate interactions.<sup>7,21</sup> Theoretically, the interaction strength between the metal adatom and the monolayer MoS<sub>2</sub> is determined by the binding energy ( $E_b$ ), the metal–metal bonding strength is obtained from the cohesive energy ( $E_c$ ) in bulk metal crystals, and the hopping barrier ( $E_{hop}$ ) describes the energy barrier that metal adatoms experience when hopping on MoS<sub>2</sub>. More uniform deposition (*i.e.*, a lower degree of clustering) for the metal adatom on MoS<sub>2</sub> is associated with a larger binding energy to cohesive energy ratio ( $E_b/E_c$ ) and a higher hopping barrier.<sup>21,22</sup>

The binding energy of metal adatoms on MoS<sub>2</sub> is calculated as the energy difference between metal–MoS<sub>2</sub> complex and isolated metal atoms and MoS<sub>2</sub>, based on a 22.10 Å × 19.14 Å super cell with a vacuum region larger than 15 Å in the direction normal to the MoS<sub>2</sub> plane. The cohesive energy of the metals is calculated based on the optimized bulk crystal. The hopping barrier is calculated by comparing the adsorption energies of the metal adatom on different high

symmetry points of the MoS<sub>2</sub> surface. The detailed study of the metal adatom hopping on MoS<sub>2</sub> is shown in Figure S2 and the related text in the Supporting Information.

These energetic and kinetic calculations provide a semiquantitative guide for the relative tendency of metal adatoms to cluster on MoS<sub>2</sub>. Figure 2d shows that Pd has the largest  $E_b/E_c$  and its  $E_{hop}$  is about 10 times larger than that of Au and Ag. These characteristics lead to wetting of Pd on MoS<sub>2</sub>, forming a uniform film morphology leading to intimate contact. The  $E_{hop}$  for Au (39 meV) and Ag (49 meV) can be overcome at room temperature since these values are close to ambient thermal energy (26 meV), thus facilitating agglomeration. Nevertheless, it is plausible to argue that the dimensionality aspect of the metal growth (*i.e.*, two-dimensional or three-dimensional growth) is mainly governed by the  $E_b/E_c$  ratio.<sup>21</sup> Therefore, the higher  $E_b/E_c$  ratio for Au than that for Ag probably leads to an ordered Au cluster distribution and an irregular Ag island distribution. In fact, the surface clustering is a far more complicated process involving many energetic and kinetic factors such as the atom–atom, cluster–cluster, and atom–cluster interaction with cluster-size dependence. As a brief summary, among these three metals, Pd behavior is therefore qualitatively different from that of Au and Ag that tend to agglomerate. Au clusters in an organized fashion, while Ag is more random, which will require a detailed kinetic modeling to fully describe.

The effects of deposited metal on electronic and phonon properties of the monolayer MoS<sub>2</sub> can be revealed by Raman spectroscopy. The Raman spectra of the three metal–MoS<sub>2</sub> contacts exhibit three main trends, as shown in Figure 3. First, after 2 nm deposition of each metal, there is always a blue shift of the A<sub>1g</sub> mode and a red shift of the E<sub>2g</sub><sup>1</sup> mode. The A<sub>1g</sub> mode represents the out-of-plane lattice vibration with sulfur atoms on both sides of Mo atoms moving in opposite directions, as illustrated in the inset of Figure 1b. The blue shift of the A<sub>1g</sub> mode can be interpreted within a classical harmonic oscillator model.<sup>23</sup> The interaction between metals and MoS<sub>2</sub> stiffens the vertical vibration of sulfur atoms. The E<sub>2g</sub><sup>1</sup> mode represents the in-plane lattice vibration with the two sulfur layers moving in the same direction collectively, opposed to the Mo movement (see inset of Figure 1b). The metal has a very large dielectric constant<sup>24</sup> and enhances the screening of the electron–electron interactions, thus weakening the planar interionic interactions. The softening of the in-plane phonon mode causes the red shift of the E<sub>2g</sub><sup>1</sup> mode.

Second, a broadening of the E<sub>2g</sub><sup>1</sup> peak is observed, which is composed of two peaks (*i.e.*, the deconvolution of the E<sub>2g</sub><sup>1</sup> peak in Figure 3a) for Au contact to MoS<sub>2</sub>. As discussed above, the AFM images in Figure 2 indicate a uniform contact between Pd and MoS<sub>2</sub> but

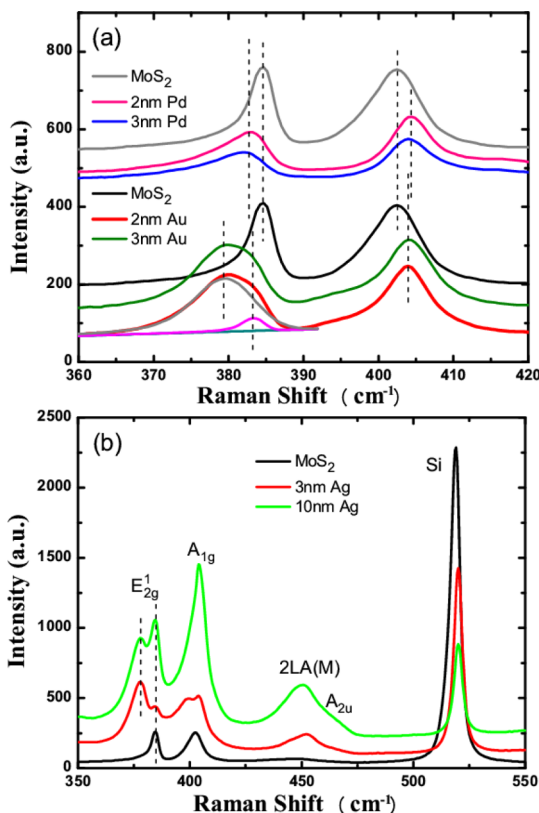


**Figure 3.** Raman spectra of single-layer MoS<sub>2</sub> covered by different thicknesses of (a) Pd and Au and (b) Ag. The samples are consecutively deposited by the same metals. For example, 3 nm Pd–MoS<sub>2</sub> is prepared from the same 2 nm Pd–MoS<sub>2</sub> sample with another 1 nm Pd deposition. (b) Wider window, exhibiting the slight SERS effect. Due to the SERS, some modes such as 2LA(M) and A<sub>2u</sub>, which are invisible in the bare monolayer MoS<sub>2</sub>, appear.

inhomogeneous contact at the exact interface between Au and MoS<sub>2</sub>. Such inhomogeneity can be described by regions with intimate contact and regions where the metal is farther spaced from the MoS<sub>2</sub> surface (*e.g.*, above the normal interface distance  $\sim 3$  Å). The combination of little lattice mismatch between Pd and MoS<sub>2</sub> (Pd is 0.5% larger than MoS<sub>2</sub>) and uniform intimate contact with MoS<sub>2</sub> leads to a uniform softening of the E<sub>2g</sub><sup>1</sup> mode ( $\sim 1.86$  cm<sup>-1</sup> red shift), resulting mostly from a metal-enhanced dielectric screening. For Au, the lattice is 5.4% larger than for MoS<sub>2</sub> and the AFM picture shows cluster formation, that is, regions in intimate contact and regions with some spacing between Au and MoS<sub>2</sub>. The responses of the MoS<sub>2</sub> phonons in these two contact regions are different, probably due to distinct strain profiles, inducing a 3.8 cm<sup>-1</sup> splitting of the E<sub>2g</sub><sup>1</sup> mode. While the whole MoS<sub>2</sub> flake is screened by the atop metal layers, resulting in the softening of the E<sub>2g</sub><sup>1</sup> mode, the parts of MoS<sub>2</sub> under the intimate contact are strained, resulting in a further softening of the E<sub>2g</sub><sup>1</sup> mode.<sup>25</sup>

We now discuss why the splitting of the E<sub>2g</sub><sup>1</sup> peak is a result of two contact scenarios rather than an incomplete Au coverage. There are two observations that rule

out the latter picture. First, there is a  $1.4\text{ cm}^{-1}$  red shift of the higher frequency  $E_{2g}^1$  peak compared to the position of the  $E_{2g}^1$  peak of the bare  $\text{MoS}_2$ . Therefore, the higher frequency  $E_{2g}^1$  peak does not correspond to the uncovered  $\text{MoS}_2$ . Second, increasing the Au deposition from 2 to 3 nm does not induce a noticeable change of the ratio of the two split peaks. In fact, the two Raman spectra (red and olive curves) in Figure 3a overlap when they are normalized to the same intensity. This evolution can only be a result of the interface inhomogeneous contact depicted in Figure 2f, which would not be affected by thicker metal deposition on top. More metal deposition on top will not modify the nature of the contact at the exact interface of a continuous film but would fill in the uncovered  $\text{MoS}_2$  given that  $\text{MoS}_2$  was not yet covered fully. Furthermore, the splitting of the  $E_{2g}^1$  peak under the Au contact also substantiates the absence of the uniform sticking layers between atop clusters and the  $\text{MoS}_2$  substrate, suggesting a VW growth mode of Au on  $\text{MoS}_2$ .

In contrast to Pd on  $\text{MoS}_2$ , Ag shows a similar behavior to Au, although with much more irregular clustering, as shown in Figure 2c. Probably due to the fact that Ag has a larger lattice mismatch (5.7% larger than  $\text{MoS}_2$ ) and a larger interface binding strength<sup>26</sup> with  $\text{MoS}_2$  than Au, the strain effect causes a  $6.38\text{ cm}^{-1}$  splitting of the  $E_{2g}^1$  mode (see Figure 3b). In addition, there is clearly a nonuniform island formation on  $\text{MoS}_2$ . In contrast to Au, the higher frequency peak of the  $E_{2g}^1$  mode of Ag– $\text{MoS}_2$  contact is identical to that of the bare  $\text{MoS}_2$  samples, indicating that the trough areas in the AFM image of the rough Ag– $\text{MoS}_2$  surface are parts of  $\text{MoS}_2$  that remained uncovered. Therefore, the lower frequency of the  $E_{2g}^1$  mode is mainly caused by  $\text{MoS}_2$  strained by Ag in intimate contact and the higher frequency by uncovered  $\text{MoS}_2$ .

The two Raman spectra for  $\text{MoS}_2$  samples with 3 and 10 nm Ag deposition do not overlap well (see Figure 3b), which supports the interpretation that the higher frequency peak of the  $E_{2g}^1$  mode for 3 nm Ag on  $\text{MoS}_2$  is mostly from the uncovered  $\text{MoS}_2$  regions. In this case, increased metal deposition changes the ratio of the covered and uncovered  $\text{MoS}_2$ , modulating the Raman spectra. To achieve the interface with a full metal coverage, we intentionally increase the amount of the Ag deposition to 10 nm. When the total thickness is 10 nm (*i.e.*, about 42 layers of Ag along [111]), the film is thick enough to cover the whole  $\text{MoS}_2$  surface. The higher frequency of the  $E_{2g}^1$  mode does not show a shift with respect to the bare  $\text{MoS}_2$ , suggesting that the existing Ag remote contact is spaced far enough from the  $\text{MoS}_2$  to reduce any Coulombic screening effect, as illustrated in Figure 2g. In fact, our quantitative DFT analysis<sup>26</sup> has shown that a larger than  $6\text{ \AA}$  interface separation is enough to almost fully decouple  $\text{MoS}_2$  from the electronic perturbation of atop metal layers.

The presence of two types of contact regions at the exact interface between  $\text{MoS}_2$  and Au (and Ag) has been well-supported. As for the reason why the  $E_{2g}^1$  Raman peaks are different at the two contact regions, one may argue the alternative possibility that the interface chemical bonding rather than the strain causes the difference. On the basis of the following two proofs, we suggest the strain as the dominant effect. First, our previous DFT modeling<sup>26</sup> shows the sequence of the metal– $\text{MoS}_2$  interface bonding strengths is  $\text{Pd} > \text{Ag} > \text{Au}$ . The wetting of  $\text{MoS}_2$  by Pd is also evidenced by the AFM images in Figure 2a. Given the assumption that the interface chemical bonding dominates the phonon behavior of  $\text{MoS}_2$  at the intimate contact region, Pd would introduce the largest amount of the  $E_{2g}^1$  mode shift. However, the Raman data show that  $\text{MoS}_2$  experiences the much larger degree of the  $E_{2g}^1$  mode shift/splitting when contacting with Ag and Au, than with Pd. The observed  $E_{2g}^1$  mode shift/splitting is therefore unlikely to be dominated by the interface chemical bonding. Second, if the interface chemical bonding dominates the phonon behavior of  $\text{MoS}_2$  at the intimate contact region, the vertical phonon mode ( $A_{1g}$ ) is expected to be more sensitively affected compared to the in-plane phonon mode ( $E_{2g}^1$ ), which is, however, not the case.

On the basis of the above observations, we suggest that the different strains in intimate contact regions and remote contact regions cause the different amounts of the  $E_{2g}^1$  mode shift, resulting in the peak splitting. Our DFT calculations (see Supporting Information Figure S5) show that the biaxial tensile strain on the bare  $\text{MoS}_2$  induces a red shift of the  $E_{2g}^1$  mode with  $4.5\text{ cm}^{-1}/\%$  strain, in an excellent agreement with the experimentally reported value  $4.5 \pm 0.3\text{ cm}^{-1}/\%$  strain.<sup>25</sup> Using this experimentally derived coefficient “ $4.5\text{ cm}^{-1}/\%$  strain”,<sup>25</sup> we infer that there is a  $\sim 0.84\%$  strain [*i.e.*,  $3.8\text{ cm}^{-1}/(4.5\text{ cm}^{-1}/\%$  strain)] at Au– $\text{MoS}_2$  intimate contact and a  $\sim 1.0\%$  strain [*i.e.*,  $(6.38 - 1.86)\text{ cm}^{-1}/(4.5\text{ cm}^{-1}/\%$  strain)] at Ag– $\text{MoS}_2$  intimate contact, assuming the contributed  $E_{2g}^1$  red shift by the Coulombic screening of Ag at intimate contact regions equals that of Pd  $1.86\text{ cm}^{-1}$ . The (111) surface has been shown to be of lowest surface energy for such face-centered cubic metals as Pd, Au, and Ag.<sup>27</sup> Hence, the metal (111) surface is more prone to be formed at metal– $\text{MoS}_2$  interfaces, although not being precisely validated yet. The lattice mismatches between  $\text{MoS}_2$  and (111) surfaces of Au (5.4%) and Ag (5.7%) are the probable main driving forces to strain the single-layer  $\text{MoS}_2$  flakes located directly underneath the bonded metal film.

The strain generated upon attachment of the metal film is tensile, possibly leading to compressive strain in the neighboring regions. However, the lack of intimate metal contact in these neighboring regions allows the lattice to move outward or even upward/downward

(i.e., become corrugated). During the dynamic metal deposition process, the boundary of MoS<sub>2</sub> is not fixed, and hence the magnitude of compressive strain in the neighboring regions is much smaller than the tensile strain in the region in intimate contact with the metal. In general, a large amount of strain ( $\geq 1\%$ ) can be formed as a result of a strong bonding between dissimilar materials with lattice mismatches, such as graphene on SiC or Si interfacing with Ge. However, a similar amount of compressive strain is hard to obtain, without the constraints induced by intimate bonding of dissimilar materials.<sup>28</sup>

A third observation in Figure 3 is also relevant to confirm the homogeneity of the Ag films, namely, the relative enhancement of the Raman signal shown in Figure 3b after Ag is deposited. It is well-known that metal particles distributed on the substrate surface enhance the Raman signal through modification of the electromagnetic field, charge-transfer effect, or surface plasmons.<sup>29</sup> In Figure 3b, the covering of metal on MoS<sub>2</sub> results in a decreased intensity of the Si peak at 520 cm<sup>-1</sup> as expected by the absorption of the thin metallic film. In contrast, the modes associated with MoS<sub>2</sub> are stronger when Ag clusters are formed. Specifically, the ratio of the MoS<sub>2</sub> peak to the Si peak is calculated for the three metals of different thickness. Figure S4 shows that the ratio increases from 0.25 to 2.40 when MoS<sub>2</sub> is covered with 3 nm thick Ag, to 1.15 when MoS<sub>2</sub> is covered with 3 nm thick Au, and drops to 0.10 when MoS<sub>2</sub> is covered with 3 nm thick Pd. This trend agrees with the different behaviors of these metals on MoS<sub>2</sub>. The uniform Pd intimate contact without clustering behavior does not induce the surface-enhanced Raman scattering (SERS) behavior, whereas the random distribution of Ag clusters induced a relatively large SERS behavior. The increase of Au deposition from 2 to 3 nm does not suppress the SERS effect, agreeing with the facts that MoS<sub>2</sub> has been fully covered with 2 nm Au, and Au assembles into clusters of saturated sizes. Therefore, more deposition of Au atop does not affect the scenarios of Au clusters at the exact interface region.

The clustered adsorption of metals such as Au and Ag has regions of intimate and remote contacts with the MoS<sub>2</sub>, which may induce inefficient electron and phonon transport<sup>8</sup> across the metal–MoS<sub>2</sub> interfaces. As discussed for the 10 nm thick Ag film, the remote contact is so spaced out that the electronic coupling between the metal and MoS<sub>2</sub> diminishes, evidenced by the unchanged peak position of the E<sub>2g</sub><sup>1</sup> mode of MoS<sub>2</sub>. To avoid a current crowding and inefficient heat dissipation, a homogeneous electrical contact is desirable for a uniform distribution of the conductive channels for electron and phonon transport.

Insertion of a two-dimensional material is a potential strategy to buffer the MoS<sub>2</sub> against the structural impact of metal electrodes (e.g., strain). Graphene is a

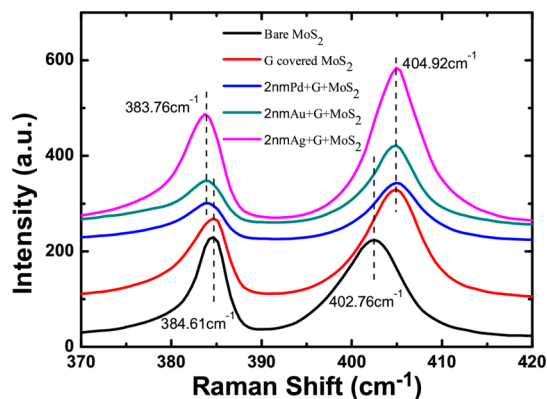


**Figure 4.** Raman spectra of the bare monolayer MoS<sub>2</sub>, the monolayer MoS<sub>2</sub> covered by graphene, and the graphene-covered MoS<sub>2</sub> with 2 nm Pd, Au, and Ag deposition on top. The proof of the successful stacking of graphene on MoS<sub>2</sub> can be found from the Raman spectrum in Figure S6. After graphene covering, the peak position of the E<sub>2g</sub><sup>1</sup> mode of the MoS<sub>2</sub> stays unchanged at 384.61 cm<sup>-1</sup> and that of the A<sub>1g</sub> mode shifts to 404.92 cm<sup>-1</sup> (with a standard deviation 0.31 cm<sup>-1</sup>), respectively. Upon three metal depositions, the A<sub>1g</sub> mode does not change, whereas the E<sub>2g</sub><sup>1</sup> mode red shifts by a similar amount (Pd, 383.74 ± 0.04 cm<sup>-1</sup>; Au, 383.91 ± 0.20 cm<sup>-1</sup>; Ag, 383.76 ± 0.31 cm<sup>-1</sup>).

chemically inert surface that can adhere to MoS<sub>2</sub> through vdW forces,<sup>30</sup> without affecting the uniformity of MoS<sub>2</sub> and introducing any gap states in MoS<sub>2</sub>. Moreover, graphene is a semimetal that is electrically active. Therefore, graphene can be used as a buffering layer between MoS<sub>2</sub> and metal films, mitigating the inhomogeneity of MoS<sub>2</sub> caused by metal deposition while maintaining an efficient electronic injection across the contact. To test this strategy, one layer of chemical vapor deposited (CVD) graphene was transferred from a copper foil onto the monolayer MoS<sub>2</sub> sample.

The presence of a graphene buffer layer between MoS<sub>2</sub> and the metal films is clearly observed by Raman spectroscopy. The spectrum in Figure S6 shows the coexistence of graphene-related and MoS<sub>2</sub>-related peaks, without evidence for strong interaction between the two layers. However, a shift is observed for the A<sub>1g</sub> mode, while the E<sub>2g</sub><sup>1</sup> mode remains fixed.

Figure 4 shows a  $\sim 2.38$  cm<sup>-1</sup> blue shift of the A<sub>1g</sub> mode of MoS<sub>2</sub> upon graphene covering, consistent with an interlayer vdW interaction that stiffens the MoS<sub>2</sub> out-of-plane phonon. It is interesting to note that the amount of the blue shift of the A<sub>1g</sub> mode of MoS<sub>2</sub> covered by graphene is larger than that directly covered by the three metals (see Figure 3). The stronger metal–MoS<sub>2</sub> interfacial bonding (than the vdW force at the graphene–MoS<sub>2</sub> interface) should cause a larger amount of blue shift of the A<sub>1g</sub> mode. However, the metal-induced in-plane tensile strain in MoS<sub>2</sub> causes a red shift of the A<sub>1g</sub> mode with a calculated coefficient “2.0 cm<sup>-1</sup>/% strain” (see Figure S5b and the related text in Supporting Information). As a result, there is an overall smaller amount of blue shift of the A<sub>1g</sub> mode at the three metal–MoS<sub>2</sub> contacts than in the graphene–MoS<sub>2</sub> stack.

The interlayer vdW interaction between graphene and MoS<sub>2</sub> is also expected to cause a minor blue shift of the E<sub>2g</sub><sup>1</sup> Raman peak. However, graphene as a low dielectric constant (2 to 15, reported in different literature<sup>31,32</sup>) material weakly screens the in-plane electron–electron interaction and otherwise softens the E<sub>2g</sub><sup>1</sup> phonon mode. Therefore, the synergetic effect is an absence of the E<sub>2g</sub><sup>1</sup> mode shift upon graphene covering. This canceling effect is believed to be the result of a stiffened in-plane phonon mode by vdW interactions and a softening of this mode by Coulombic screening.

When 2 nm of Pd, Au, and Ag is deposited on graphene/MoS<sub>2</sub>, as shown in Figure 4, there is no evolution of the A<sub>1g</sub> peak, which is a strong indicator of the physical decoupling between deposited metals and MoS<sub>2</sub>. In contrast, there is a red shift (0.85 cm<sup>-1</sup>) of the E<sub>2g</sub><sup>1</sup> peaks without peak splitting upon metal deposition, which is similar for all three metals. This red shift implies a strong electronic coupling between the metal and MoS<sub>2</sub>, which is due to a metal-enhanced Coulombic screening. The absence of the peak splitting is consistent with an absence (*i.e.*, a uniform profile) of strain throughout the whole MoS<sub>2</sub> film, even for the Ag film that clearly clusters on graphene (see Figure S7). This phenomenon highlights the role of the graphene as a buffer layer to eliminate deleterious

inhomogeneities in deposited metal films that tend to cluster on MoS<sub>2</sub>.

## CONCLUSION

In summary, the adsorption of metal atoms on MoS<sub>2</sub> depends on the specific metallic elements, similarly to graphene. Pd wets MoS<sub>2</sub>, forming a uniform intimate contact, while the adsorption of Au and Ag is inhomogeneous, with a tendency to cluster into tens of nanometer-sized features. The agglomeration of Au and Ag into clusters results in two types of interfaces: regions with (i) intimate contact and (ii) with a spacing (*i.e.*, remote contact) between the metal and MoS<sub>2</sub> at edges of metal clusters, creating inhomogeneity. Such inhomogeneity in contacts is likely to deteriorate the electron injection efficiency and to introduce overheating due to electron crowding mainly through the intimate contact points with less heat dissipation of the MoS<sub>2</sub> phonon into metal. Graphene is shown to provide an effective buffer layer between all three metal electrodes and MoS<sub>2</sub>. Graphene not only eliminates the deleterious effects of inhomogeneous contact on MoS<sub>2</sub> but also fosters good electron injection into MoS<sub>2</sub> (*i.e.*, a strong electronic coupling between the atop metal electrode and MoS<sub>2</sub>) thanks to its superior electrical properties.

## EXPERIMENTAL AND THEORETICAL METHODS

**Monolayer MoS<sub>2</sub> Preparation.** A MoS<sub>2</sub> powder source (0.1 g, Alfa Aesar, 99% purity) in an alumina boat is placed in the center of a horizontal quartz tube furnace. The insulating substrate (285 nm SiO<sub>2</sub>/Si) is cleaned in acetone, isopropyl alcohol, and deionized water and is placed downstream far from the oven center in a cooler zone (at ~650 °C during growth). The tube is initially pumped to a base pressure of 20 mTorr and flushed with the Ar carrier gas (~20 sccm) repeatedly at room temperature to remove oxygen contamination. With the carrier gas flowing and the pressure maintained at ~20 Torr, the furnace temperature is then increased to ~900 °C (~35 °C/min) and held there for 15–20 min before being allowed to cool naturally. Monolayer MoS<sub>2</sub> flakes are physical vapor deposited on the SiO<sub>2</sub> substrate.

**Metal Deposition.** Metals are e-beam-evaporated on the MoS<sub>2</sub> samples by Temescal in a 2 × 10<sup>-6</sup> Torr vacuum. Before each deposition, metals are heated 5 min by a 0.1–0.2 A higher current than the emission current during the normal metal deposition to remove surface contamination or oxides. The deposition rates are controlled between 0.1 and 0.2 Å/s. Quartz crystal monitor is used to estimate the deposition thickness. Therefore, the recorded thickness is the maximum real thickness of metal deposited on MoS<sub>2</sub>, considering the inertness of MoS<sub>2</sub>.

**Graphene Transfer.** Details of CVD growth of large-area single-layer graphene on a copper foil and the PMMA-aided wet transfer of the graphene onto MoS<sub>2</sub>/SiO<sub>2</sub> can be found in our previous work.<sup>33,34</sup> The only modification of the graphene transfer process is that the heating temperature on the hot plate for smoothing the PMMA/graphene stacks is lowered to 150 °C, preventing the possible damage to the underlying MoS<sub>2</sub> flakes. After the 2.5 h in acetone, the PMMA residues are further cleaned by the thermal annealing in N<sub>2</sub> atmosphere at 200 °C for 2 h.

**Raman Measurements.** Raman spectra acquisition is done with an Alpha visible Raman spectrometer from Thermo Nicolet.

On each sample, at least 7 flakes with more than 7 different spots on each flake are sampled. The laser excitation is at 532 nm wavelength. The objective lens is 100× magnification. High resolution is adopted with 0.24 cm<sup>-1</sup> resolution. The Raman laser power effect<sup>35</sup> is examined from 16 to 65% (see the Supporting Information), and the 25% power is used in the systematic experiments of this work. Each spectrum is an average of 20 acquisitions, with each acquisition lasting 2 s, to minimize the noise-to-signal ratio.

**Density Functional Theory Calculations.** As shown in Figure S2, the super cell for metal adsorbed on MoS<sub>2</sub> is a 22.10 Å × 19.14 Å rectangle, with 20 Å in the direction perpendicular to the MoS<sub>2</sub> plane. Therefore, there is a larger than 15 Å vacuum region, considering the different adsorption heights of different metal atoms. The calculations are performed by VASP<sup>36</sup> with projector-augmented wave (PAW) pseudopotential<sup>37</sup> with generalized gradient approximation (GGA) of Perdew–Burke–Ernzerhof (PBE) functional to describe the exchange correlation. Spin polarization is necessary for gaining the accurate total energies since single metal atoms are studied. The ionic relaxation stops when the remnant force on each atom below 0.01 eV/Å. The energy cutoff is chosen at 400 eV, and the electronic optimization stops when the total energies of neighboring optimization loops differ below 10<sup>-4</sup> eV. The Monkhorst–Pack k-point sampling in Brillouin zone (BZ) is  $\Gamma$ -centered with 4 × 4 × 1 in electronic optimization. The calculation of the  $\Gamma$ -point vibration frequency in strained MoS<sub>2</sub> is also done by VASP with PBE functional.

**Conflict of Interest:** The authors declare no competing financial interest.

**Acknowledgment.** The work at UT Dallas was supported partly by NSF (CHE-1300180), and the Center for Low Energy Systems Technology (LEAST), one of six centers supported by the STARnet phase of the Focus Center Research Program (FCRP), a Semiconductor Research Corporation program

sponsored by MARCO and DARPA. The MoS<sub>2</sub> synthesis performed at the University of Washington (C.H., D.C., and X.X.) was supported by U.S. DoE, BES, Materials Science and Engineering Division.

**Supporting Information Available:** A magnified AFM image of 2 nm Au on monolayer MoS<sub>2</sub>; DFT study of adsorption and hopping of metal adatoms on monolayer MoS<sub>2</sub>; Raman laser power dependence of Raman spectra of monolayer MoS<sub>2</sub>; surface-enhanced Raman scattering study of the three meals on MoS<sub>2</sub>; DFT calculated biaxial tensile strain dependence of the MoS<sub>2</sub> E<sub>2g</sub><sup>1</sup> and A<sub>1g</sub> modes frequencies; Raman spectrum of a graphene-covered MoS<sub>2</sub> sample; AFM image of 2 nm Ag on graphene on MoS<sub>2</sub>. This material is available free of charge via the Internet at <http://pubs.acs.org>.

## REFERENCES AND NOTES

- Radisavljevic, B.; Radenovic, A.; Brivio, J.; Giacometti, V.; Kis, A. Single-Layer MoS<sub>2</sub> Transistors. *Nat. Nanotechnol.* **2011**, *6*, 147–150.
- Das, S.; Chen, H. Y.; Penumatcha, A. V.; Appenzeller, J. High Performance Multilayer MoS<sub>2</sub> Transistors with Scandium Contacts. *Nano Lett.* **2013**, *13*, 100–105.
- Fuhrer, M. S.; Hone, J. Measurement of Mobility in Dual-Gated MoS<sub>2</sub> Transistors. *Nat. Nanotechnol.* **2013**, *8*, 146–147.
- Wang, H.; Yu, L. L.; Lee, Y. H.; Shi, Y. M.; Hsu, A.; Chin, M. L.; Li, L. J.; Dubey, M.; Kong, J.; Palacios, T. Integrated Circuits Based on Bilayer MoS<sub>2</sub> Transistors. *Nano Lett.* **2012**, *12*, 4674–4680.
- Neal, A. T.; Liu, H.; Gu, J. J.; Ye, P. D. Metal Contacts to MoS<sub>2</sub>: A Two-Dimensional Semiconductor; *Device Research Conference*, University Park, TX, **2012**; pp 65–66.
- Qiu, H.; Pan, L. J.; Yao, Z. N.; Li, J. J.; Shi, Y.; Wang, X. R. Electrical Characterization of Back-Gated Bi-layer MoS<sub>2</sub> Field-Effect Transistors and the Effect of Ambient on Their Performances. *Appl. Phys. Lett.* **2012**, *100*, 123104.
- Zhang, Y.; Franklin, N. W.; Chen, R. J.; Dai, H. J. Metal Coating on Suspended Carbon Nanotubes and Its Implication to Metal-Tube Interaction. *Chem. Phys. Lett.* **2000**, *331*, 35–41.
- Mao, R.; Kong, B. D.; Gong, C.; Xu, S.; Jayasekera, T.; Cho, K.; Kim, K. W. First-Principles Calculation of Thermal Transport in Metal/Graphene Systems. *Phys. Rev. B* **2013**, *87*, 165410.
- Zhou, Z. H.; Gao, F.; Goodman, D. W. Deposition of Metal Clusters on Single-Layer Graphene/Ru(0001): Factors that Govern Cluster Growth. *Surf. Sci.* **2010**, *604*, L31–L38.
- N'Diaye, A. T.; Gerber, T.; Busse, C.; Myslivecek, J.; Coraux, J.; Michely, T. A Versatile Fabrication Method for Cluster Superlattices. *New J. Phys.* **2009**, *11*, 103045.
- Luo, Z. T.; Somers, L. A.; Dan, Y. P.; Ly, T.; Kybert, N. J.; Mele, E. J.; Johnson, A. T. C. Size-Selective Nanoparticle Growth on Few-Layer Graphene Films. *Nano Lett.* **2010**, *10*, 777–781.
- Gong, C.; Lee, G.; Shan, B.; Vogel, E. M.; Wallace, R. M.; Cho, K. First-Principles Study of Metal–Graphene Interfaces. *J. Appl. Phys.* **2010**, *108*, 123711.
- Khomyakov, P. A.; Giovannetti, G.; Rusu, P. C.; Brocks, G.; van den Brink, J.; Kelly, P. J. First-Principles Study of the Interaction and Charge Transfer between Graphene and Metals. *Phys. Rev. B* **2009**, *79*, 195425.
- Gong, C.; Hinojos, D.; Wang, W. C.; Nijem, N.; Shan, B.; Wallace, R. M.; Cho, K. J.; Chabal, Y. J. Metal–Graphene–Metal Sandwich Contacts for Enhanced Interface Bonding and Work Function Control. *ACS Nano* **2012**, *6*, 5381–5387.
- Popov, I.; Seifert, G.; Tomanek, D. Designing Electrical Contacts to MoS<sub>2</sub> Monolayers: A Computational Study. *Phys. Rev. Lett.* **2012**, *108*, 156802.
- Chen, W.; Santos, E. J. G.; Zhu, W. G.; Kaxiras, E.; Zhang, Z. Y. Tuning the Electronic and Chemical Properties of Monolayer MoS<sub>2</sub> Adsorbed on Transition Metal Substrates. *Nano Lett.* **2013**, *13*, 509–514.
- Wu, S. F.; Huang, C. M.; Aivazian, G.; Ross, J. S.; Cobden, D. H.; Xu, X. D. Vapor–Solid Growth of High Optical Quality MoS<sub>2</sub> Monolayers with Near-Unity Valley Polarization. *ACS Nano* **2013**, *7*, 2768–2772.
- Lee, C.; Yan, H.; Brus, L. E.; Heinz, T. F.; Hone, J.; Ryu, S. Anomalous Lattice Vibrations of Single- and Few-Layer MoS<sub>2</sub>. *ACS Nano* **2010**, *4*, 2695–2700.
- Li, H.; Zhang, Q.; Yap, C. C. R.; Tay, B. K.; Edwin, T. H. T.; Olivier, A.; Baillargeat, D. From Bulk to Monolayer MoS<sub>2</sub>: Evolution of Raman Scattering. *Adv. Funct. Mater.* **2012**, *22*, 1385–1390.
- Gong, C.; Zhang, H.; Wang, W.; Colombo, L.; Wallace, R. M.; Cho, K. Band Alignment of Two-Dimensional Transition Metal Dichalcogenides: Application in Tunnel Field Effect Transistors. *Appl. Phys. Lett.* **2013**, *103*, 053513.
- Liu, X. J.; Hupalo, M.; Wang, C. Z.; Lu, W. C.; Thiel, P. A.; Ho, K. M.; Tringides, M. C. Growth Morphology and Thermal Stability of Metal Islands on Graphene. *Phys. Rev. B* **2012**, *86*, 081414.
- Liu, X. J.; Wang, C. Z.; Hupalo, M.; Lu, W. C.; Tringides, M. C.; Yao, Y. X.; Ho, K. M. Metals on Graphene: Correlation between Adatom Adsorption Behavior and Growth Morphology. *Phys. Chem. Chem. Phys.* **2012**, *14*, 9157–9166.
- Li, T. S.; Galli, G. L. Electronic Properties of MoS<sub>2</sub> Nanoparticles. *J. Phys. Chem. C* **2007**, *111*, 16192–16196.
- Hwang, C.; Siegel, D. A.; Mo, S. K.; Regan, W.; Ismach, A.; Zhang, Y. G.; Zettl, A.; Lanzara, A. Fermi Velocity Engineering in Graphene by Substrate Modification. *Sci. Rep.* **2012**, *2*, 590.
- Conley, H. J.; Wang, B.; Ziegler, J. I.; Haglund, R. F.; Pantelides, S. T.; Bolotin, K. I. Bandgap Engineering of Strained Monolayer and Bilayer MoS<sub>2</sub>. *Nano Lett.* **2013**, *13*, 3626–3630.
- Gong, C.; Colombo, L.; Wallace, R. M.; Cho, K. *Nano Lett.*, submitted.
- Skriver, H. L.; Rosengaard, N. M. Surface-Energy and Work Function of Elemental Metals. *Phys. Rev. B* **1992**, *46*, 7157–7168.
- Lee, J. E.; Ahn, G.; Shim, J.; Lee, Y. S.; Ryu, S. Optical Separation of Mechanical Strain from Charge Doping in Graphene. *Nat. Commun.* **2012**, *3*, 1024.
- Mock, J. J.; Barbic, M.; Smith, D. R.; Schultz, D. A.; Schultz, S. Shape Effects in Plasmon Resonance of Individual Colloidal Silver Nanoparticles. *J. Chem. Phys.* **2002**, *116*, 6755–6759.
- Britnell, L.; Gorbachev, R. V.; Jalil, R.; Belle, B. D.; Schedin, F.; Mishchenko, A.; Georgiou, T.; Katsnelson, M. I.; Eaves, L.; Morozov, S. V.; *et al.* Field-Effect Tunneling Transistor Based on Vertical Graphene Heterostructures. *Science* **2012**, *335*, 947–950.
- Elias, D. C.; Gorbachev, R. V.; Mayorov, A. S.; Morozov, S. V.; Zhukov, A. A.; Blake, P.; Ponomarenko, L. A.; Grigorieva, I. V.; Novoselov, K. S.; Guinea, F.; *et al.* Dirac Cones Reshaped by Interaction Effects in Suspended Graphene. *Nat. Phys.* **2011**, *7*, 701–704.
- Santos, E. J. G.; Kaxiras, E. Electric-Field Dependence of the Effective Dielectric Constant in Graphene. *Nano Lett.* **2013**, *13*, 898–902.
- Pirkle, A.; Chan, J.; Venugopal, A.; Hinojos, D.; Magnuson, C. W.; McDonnell, S.; Colombo, L.; Vogel, E. M.; Ruoff, R. S.; Wallace, R. M. The Effect of Chemical Residues on the Physical and Electrical Properties of Chemical Vapor Deposited Graphene Transferred to SiO<sub>2</sub>. *Appl. Phys. Lett.* **2011**, *99*, 122108.
- Gong, C.; Floresca, H. C.; Hinojos, D.; McDonnell, S.; Qin, X.; Hao, Y.; Jandhyala, S.; Mordi, G.; Kim, J.; Colombo, L.; *et al.* Rapid Selective Etching of PMMA Residues from Transferred Graphene by Carbon Dioxide. *J. Phys. Chem. C* **2013**, *117*, 23000–23008.
- Najmaei, S.; Liu, Z.; Ajayan, P. M.; Lou, J. Thermal Effects on the Characteristic Raman Spectrum of Molybdenum Disulfide (MoS<sub>2</sub>) of Varying Thicknesses. *Appl. Phys. Lett.* **2012**, *100*, 013106.
- Kresse, G.; Furthmüller, J. Efficiency of *Ab-Initio* Total Energy Calculations for Metals and Semiconductors Using a Plane-Wave Basis Set. *Comput. Mater. Sci.* **1996**, *6*, 15–50.
- Bloch, P. E. Projector Augmented-Wave Method. *Phys. Rev. B* **1994**, *50*, 17953–17979.